



Revealing the role of ripples in phonon modes for MoS₂ and MoSe₂: Insights from molecular dynamics and machine learning

Journal:	<i>Physical Chemistry Chemical Physics</i>
Manuscript ID	CP-ART-01-2025-000163.R1
Article Type:	Paper
Date Submitted by the Author:	26-Apr-2025
Complete List of Authors:	Garcia de Souza, Gabriel Bruno; Universidade Federal de Minas Gerais, Physics; University of Georgia, Center for Simulational Physics Bennett Hancock, Steven; Johns Hopkins University Applied Physics Laboratory; University of Georgia, Center for Simulational Physics Landau, David Paul; University of Georgia, Center for Simulational Physics Abate, Yohannes; University of Georgia, Physics and Astronomy de Paiva, Rosângela; Universidade Federal de São João del-Rei, Departamento de Estatística, Física e Matemática - Campus Alto Paraopeba Nascimento, Von Braun; Universidade Federal de Minas Gerais, Departamento de Física

Cite this: DOI: 00.0000/xxxxxxxxxx

Revealing the role of ripples in phonon modes for MoS₂ and MoSe₂: Insights from molecular dynamics and machine learning[†]

Gabriel Bruno G. de Souza,^{*a,b} Steven B. Hancock,^c David Paul Landau,^b Yohannes Abate,^d Rosângela de Paiva^e and Von Braun Nascimento^a

Received Date
Accepted Date

DOI: 00.0000/xxxxxxxxxx

Interatomic potentials for single-layer MoS₂ and MoSe₂ were developed by training an Artificial Neural Network with a reference data set generated using Density Functional Theory. High accuracy was obtained for the phonon dispersion as well as a direct correspondence of the predicted Raman and infrared (IR) active modes (between 100 cm⁻¹ and 600 cm⁻¹) with Molecular Dynamics results. The ability to perform simulations with thousands of atoms allowed our system to accommodate spontaneous fluctuations in height and ripples propagating in the material. As a result of these ripples, our simulations suggest the existence of IR activity in the E' and A₂' modes with inverted polarization, as well as the presence of IR activity at frequencies close to E'' and A₁', which are generally considered IR-inactive. The rippling of the system is expected to be responsible for breaking the 3-fold rotational symmetry around the z-axis of the material, resulting in non-trivial IR modes.

1 Introduction

Transition Metal Dichalcogenides (TMDs) have the stoichiometry MX₂ with M being a transition metal (e.g., M = Mo, W...) and X belonging to the oxygen family (e.g., X = S, Se, Te). Single-layer (SL) TMDs present unique behavior^{1,2}, with potential optoelectronic applications. Notably, SL-MoS₂ is known for having a direct bandgap suitable for light absorption in the visible range of 1.88 eV while its bulk counterpart has an indirect bandgap of 1.29 eV³. Furthermore, excitonic effects with strong binding energies⁴ play a major role in its optical properties. This system with its unique optical response can be leveraged in nanoscale transistors⁵ and several photoactive devices. MoS₂ is also known to have promising thermal properties due to carrier transport⁶. Similarly, MoSe₂ is known to share such optical properties with MoS₂ by having a direct bandgap of 1.63 ± 0.01 eV⁷.

Molecular Dynamics (MD) simulation is a well-known tool for

studying structural and dynamical properties of TMDs that which often strongly depend on the temperature of the system⁸⁻¹⁰ such as thermal conductivity and expansion coefficients which can be compared with experimental results. However, one of the main limitations of using MD simulations to explain real experiments is the accuracy of the interaction potentials/force fields between atoms in the simulation. Potentials with a complex functional form are usually developed in order to close the gap between experiment and simulation, e.g., Tersoff for carbon¹¹, TIP3P for water¹²⁻¹⁴, Vashishta for Silica¹⁵ and the Embedded Atom Method for metallic systems¹⁶. A widely employed potential for MoS₂ is the Stillinger-Weber proposed by Jiang *et. al.*^{17,18} to reproduce phonon dispersion but the breaking and formation of bonds is better described by the ReaxFF potential¹⁹, which makes the work of simulating SL-MoS₂ a challenging prospect as one needs to select which potential is most suitable for the desired property, an indication of the non-transferability of these potentials such that their lack of accuracy can raise the aforementioned problems. Ab initio molecular dynamics (aiMD) could theoretically solve this but the calculations are so computationally expensive that only systems with at most a few hundred atoms could be explored. One way to overcome these issues is to use Machine Learning (ML) methods to develop potentials based on data generated using Density Functional Theory (DFT), also known as Machine Learning Force Fields (MLFFs)²⁰. The main idea is to generate a reference data set with DFT calculations of several structures and train a machine learning model (e.g. kernel based or neural networks) to reproduce its results within the desired accuracy. After training,

^a Departamento de Física, Universidade Federal de Minas Gerais (UFMG), Belo Horizonte – MG, Brasil, 31270-901; E-mail: gbsouza1997@ufmg.br; vnascimento.ufmg@gmail.com

^b Center for Simulational Physics, University of Georgia (UGA), Athens – GA, USA, 30602

^c Johns Hopkins Applied Physics Laboratory (APL), Laurel - MD, USA, 20723

^d Department of Physics and Astronomy, University of Georgia (UGA), Athens – GA, USA, 30602

^e Departamento de Estatística, Física e Matemática, Universidade Federal de São João del Rei (UFSJ), Ouro Branco – MG, Brasil, 36495-000

[†] Electronic supplementary information (ESI) available. See DOI: 00.0000/xxxxxxxxxx/

the model will not have a specific functional form like the conventional force fields but will be able to reflect the DFT effective motion patterns with an arbitrary accuracy and the reliability of the ML model will be related with the structures included in the data set. Therefore, simulations using MLFFs will have an accuracy similar to aiMD with much less computational cost. To some extent, lattice dynamics offer a solid theoretical background to several optical experiments such as infrared (IR) terahertz (THz) absorption as well as Raman scattering²¹. On a crystalline system, the lattice dynamics of a system is well described by its phonon dispersion and a common criterion to test the reliability of a force field (conventional or ML based) is to calculate its phonon dispersion and compare with ab initio calculations or experimental results²².

Moreover, because SL-MoS₂ and MoSe₂ are ordered periodic 2D systems, one would expect them to be thermodynamically unstable at finite temperatures according to the Mermin Theorem²³, and that thermal fluctuations would inhibit any kind of long-range order necessary in a 2D crystal. However, subsequent studies have shown that such fluctuations can be suppressed by an anharmonic coupling between the "bend" and "stretch" acoustic modes^{24,25} and that such materials could be stable at finite temperature as long as they present large ripples. In graphene such ripples tend to be between 50 and 100 Å in lateral size and around 5 to 10 Å in height²⁶ while in MoS₂ those numbers vary between 60 to 100 Å and 6 to 10 Å respectively²⁷. Also, ripples have an important role on the thermal expansion properties²⁸ and several efforts are underway to determine the structure of ripples through image reconstruction²⁹. Here, we present two MLFFs developed for SL-MoS₂ and MoSe₂, we validate our models by reproducing experimental dielectric spectra results at low frequencies such as THz absorption with MD simulations and present results on how the ripples propagating through the system affect the spectra according to our MLFFs. In our simulations, we observed that these ripples are responsible for new peaks in the dielectric spectra beyond the usual peaks pertaining to E' and A''₂ modes, including ones next to phonon modes known to be IR inactive. This paper is structured as follows: in Sec. 2 we detail all models and methods used in this study, Sec. 3 show our results and have the main discussion, and we conclude in Sec. 4. Sec. 2 will be divided into three different subsections: in 2.1 we will describe the DFT calculations used to generate the reference data set, on 2.2 we will show the machine learning method selected to produce the MLFF and on 2.3 we will present the MD simulations and data analysis used on this study. Furthermore, Sec. 3 will also be divided into three subsections: the discussions about the development, accuracy and testing of the MLFFs for MoS₂ and MoSe₂ will be on Secs. 3.1 and 3.2 respectively while Sec 3.3 contains all the discussions about the role of thermal ripples on the THz spectra and the phonon modes for both compounds.

2 Methodology

2.1 DFT Calculations & Data set

In order to generate our data set, we performed self-consistent first-principle calculations using the plane wave pseudopoten-

tial method within the density functional formalism as implemented in the Quantum Espresso code³⁰⁻³². We used Optimized Norm-Conserving Vanderbilt (ONCV) pseudopotentials^{33,34} to treat the interaction between the atomic core and the valence electrons and the PBE generalized gradient approximation for the exchange-correlation potentials³⁵. A Monkhorst-Pack grid of $6 \times 6 \times 1$ was used for the integration on the Brillouin-zone and a kinetic energy cutoff of 70 Ry and 280 Ry was used for the wavefunctions and charge density respectively (see Figure S1 in ESI†). The hexagonal primitive cell (see: red diamond on Figure 1a) relaxation was achieved when the total force on the unit cell was less than 5.0×10^{-3} eV/Å. A vacuum region of 20 Å is set to ensure negligible spurious interactions between neighboring replicas. As a result of structure relaxation, the optimized lattice constant (indicated as \mathbf{a}_0 on Figure 1a) of SL-MoS₂ was 3.186 Å, which has a 0.79% error with respect to the experimental value of 3.16 Å³⁶. The Mo-S relaxed distance (shown as $d_{\text{Mo-X}}$ at 1b) was calculated to be 2.414 Å and the S-Mo-S angle as 80.76° (shown as θ at 1b). For MoSe₂, we adopted a cutoff radius of 40 Ry for the wave functions and 160 Ry for the charge density (see Figure S1 in ESI†). The optimized lattice constant of SL-MoSe₂ was 3.32 Å, which has a 0.91% error with respect to the experimental value of 3.29 Å³⁷. The Mo-Se relaxed distance was calculated to be 2.541 Å and the Se-Mo-Se angle was calculated to be of 82.12°. Those are the main parameters of the cell optimization and small displacements around those equilibrium positions are expected to have restoring forces.

The initial set of reference structures for the MLFF construction was generated by systematically distorting the ideal structure. The lattice constants of the crystal structures were scaled within a range of $\pm 45\%$ around the equilibrium value on the xy

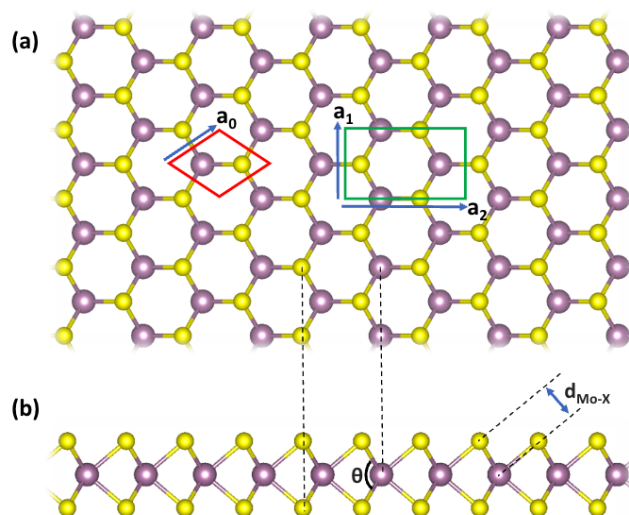


Figure 1 Top (a) and side (b) views of SL MoX₂ (X = S, Se). Mo is indicated in purple while X is in yellow. The red diamond indicates the hexagonal primitive cell with the lattice parameter a_0 indicated as an arrow. The green rectangle shows the rectangular unit cell with the arrows indicating the parameters $|a_1| = |a_0|$ and $|a_2| = |a_0|\sqrt{3}$. The distance between Mo and X is shown by $d_{\text{Mo-X}}$ and the angle between X-Mo-X is shown by θ .

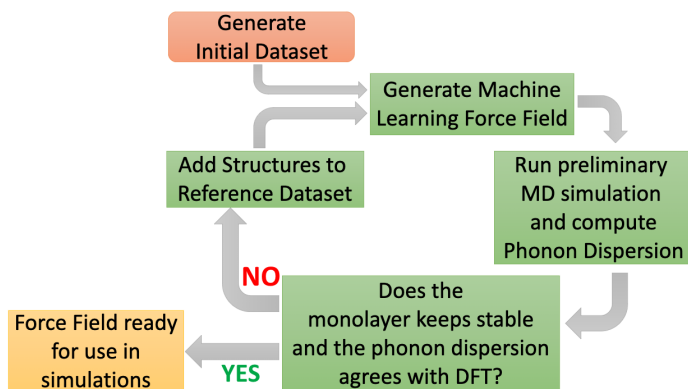


Figure 2 Flowchart of the adopted methodology for construction, improvement and utilization of the Machine Learning Force Fields (MLFFs) generated in this work.

and z directions⁸. To get a sample of the atomic forces, for each pair (xy, z) of scale percentages we ran 3 to 5 different DFT calculations with atomic positions randomly displaced about their equilibrium positions with displacement amplitudes in the range of $0.01\text{Å} - 0.1\text{Å}$. This initial set is used to generate a preliminary MLFF which is used to calculate the phonon dispersion and run a preliminary MD simulation to check the stability of the system. As we proceed to satisfy both criterion, additional structures were added to the initial data set. We shift atoms along lines corresponding to normal modes on various points of the Brillouin zone to ensure that our database contains sufficient information to reproduce the phonon dispersion, especially in the vicinity of the Γ point where the preliminary calculations often presented dynamical instabilities. This data collection method is known as normal mode sampling²⁰ and the overall workflow is illustrated at Figure 2. In total, the reference data set comprises a total of 5259 structures for MoS_2 and 6187 for MoSe_2 , each of which with has the number of atoms in the unit cell ranging from 3 to 48.

2.2 Machine Learning Methods

Here we used an Artificial Neural Network (ANN) as implemented in the Atomistic Energy Network (`ænet`)^{38,39} package based on descriptors represented on the Chebyshev basis⁴⁰. This package has tools for generating, training and testing ANNs. In our model, we considered interactions up to a certain cutoff radius r_{cut} , which are represented by an ANN as shown schematically in Figure 3. The ANN returns the potential energy $E_{\xi}(\mathbf{r})$ of one atom in the system (atom ξ) based on the position of itself and its neighbors within the cutoff. These positions must be represented in a set of coordinates $\{x_0^i\}$ that is invariant with respect to translation, rotation and exchange of atoms, which are the descriptors indicated at Figure 3 and are used as the input layer for the MLFF.

In addition to the parameters that are determined during the training process of a machine learning model, e.g., the weights

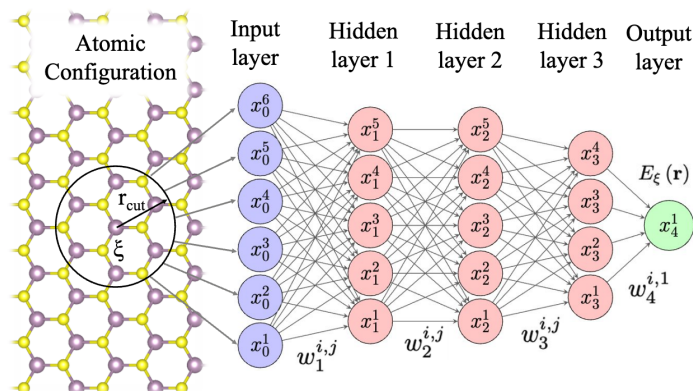


Figure 3 Schematic representation of a MLFF that consists of an input layer, three hidden layers and an output layer. The configuration of neighbors around atom ξ within a cutoff r_{cut} is transformed to a descriptor x_0^i ($i = 1, \dots, 6$) and used as the input to the MLFF. Arrows connecting nodes in adjacent layers represents weights. Biases and activation functions are not shown for simplicity. The selection of number of nodes and layers in this figure are only for illustration purposes.

$w_j^{i,j}$ in ANNs present in Figure 3, most of models contain hyperparameters that are chosen before training and do not change during it. Their choice can affect the accuracy of model and its behavior during simulations since a model with too few parameters may not capture all desired features in the database. For our ANNs, there are two different types of hyperparameters. The first set is related to the representation of the local structure environment of the system, also known as "fingerprints", which must be defined for both Mo and S (Se) atom types. We have used the same hyperparameters to define the descriptors for all atom types: a radial r_{cut} of 9.0Å , a radial order expansion of 16, an angular r_{cut} of 8.0Å and an angular order expansion of 8. The second set of hyperparameters is the number of hidden layers that connects the input layer to the output layer as well as the number of nodes in each. Moreover, an activation function is defined between two successive layers. Here, for MoS_2 we built an ANN composed by 2 layers with 24 nodes followed by 2 layers with 20 nodes (a total of 4 hidden layers), using hyperbolic tangent as the activation function. For MoSe_2 we built an ANN composed by 2 layers with 20 nodes followed by 2 layers with 16 nodes and the same activation function. We also tested neural networks with 2 and 3 hidden layers. However, none of them were able to reproduce the desired dynamical properties of the studied systems. Of the diverse number of nodes and layers that were tried, those architectures showed the best results. On the training process, the cost function chosen to be minimized is the root mean squared error (RMSE):

$$\text{RMSE} = \sqrt{\frac{1}{N_{Ref}} \sum_{\sigma} [E^{MLFF}(\sigma) - E^{DFT}(\sigma)]^2} \quad (1)$$

with N_{Ref} being the number of reference structures and σ indicating each structure in the data set. We employed the Broyden-Fletcher-Goldfarb-Shanno (BFGS) method for weight optimization^{41,42}. The reference data set was split into a training set of 80% and a testing set of 20% to check the prediction capability.

§ The justification for the large variation of the lattice constant is that our database needs to contain information for when atoms are very close ($r \rightarrow 0$) and very far ($r \rightarrow \infty$) from each other to make our MLFFs reproduce those conditions.

A test of the accuracy and validation of the MLFFs can be found in Sec. 4.2 of ESI†.

2.3 Molecular Dynamics Simulations

All MD simulations in this study were made using the Large-scale Atomic/Molecular Massively Parallel Simulator (LAMMPS)⁴³ with the assistance of a module that allows Neural Networks generated with the \ae net package to be used on LAMMPS simulations as "pair styles"⁴⁴. The procedure to obtain the complex dielectric spectra at THz frequencies is based on expressing the dielectric spectra as a Fourier transform of the average total dipole moment correlation function on time domain⁴⁵:

$$\varepsilon(\omega) = 1 + \frac{1}{3\varepsilon_0 V k_B T} \left[\langle \mathbf{M}^2 \rangle + i\omega \int_0^\infty \langle \mathbf{M}(t) \cdot \mathbf{M}(0) \rangle e^{i\omega t} dt \right] \quad (2)$$

where $\mathbf{M} = \mathbf{M}(t)$ indicates total dipole moment of system, ε_0 is the vacuum permittivity, V is the volume and ω the angular frequency. For these simulations, we used a timestep of $dt = 1$ fs within the following scheme: the first 250,000 steps were performed with the Nosé-Hoover Thermostat (NVT ensemble) at a chosen temperature to equilibrate the system and, after that, the thermostat is turned off and the simulations were carried out in the NVE ensemble, which is required to obtain dynamical properties. Since the Nosé-Hoover Thermostat is based on an extended Lagrangian responsible for coupling the system to an external heat-bath⁴⁶, oscillations of the coupled heat-bath could affect the correlation functions needed in Eq. 2. By switching from the NVT to the NVE ensemble, with the appropriate amount of equilibration steps, we were able to prevent these "virtual" oscillations from influencing the final result. After 8,000 steps to equilibrate the system in the NVE ensemble, the subsequent 3,992,000 additional NVE steps were conducted to obtain individual $\mathbf{M}(t) \cdot \mathbf{M}(0)$ functions where t ranges from 0 to 22 ps. Then the overlap approach was used to increase correlation between successive samples, reducing the noise in the Fourier transform^{10,47}. These individual functions were averaged to obtain the main correlation function of dipole moment which was used to obtain the dielectric spectra of the material. To obtain the error bars in our calculations, all $\mathbf{M}(t) \cdot \mathbf{M}(0)$ functions were partitioned in 10 different groups, each one of them giving one estimate to the dielectric function. Then, those estimates were averaged for the final results. The simulation cell was a rectangular supercell (see green rectangle at Figure 1) with a total of 16320 atoms and dimensions $68 \mathbf{a}_1 \times 40 \mathbf{a}_2$ ($\mathbf{a}_1 = \mathbf{a}_0$ and $\mathbf{a}_2 = \mathbf{a}_0 \sqrt{3}$). This size was adopted to minimize finite size effects and simulations with larger lattices did not improve the results.

3 Results & Discussion

3.1 MoS₂

3.1.1 Phonon properties

Figure 4 shows the results for the phonon dispersion calculated with the developed MLFF for MoS₂ in this study. The comparison with DFT in Figure 4a has the purpose of verify how accurately the MLFF reproduces the data on the reference set. We can see

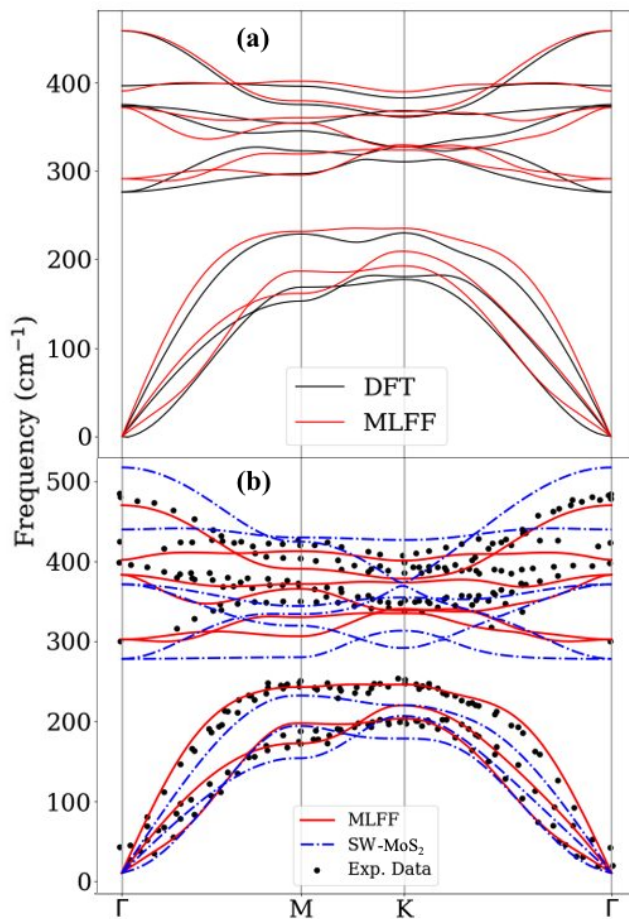


Figure 4 Phonon dispersion of MoS₂ along high symmetry directions Γ -M-K- Γ for MLFF, DFT calculations, Stillinger-Weber (SW-MoS₂) potential estimation and Inelastic X-Ray Scattering data.

that all the main features of the DFT dispersion are reproduced by our MLFF for both the optical and acoustic branches, indicating that our model "learned" the main motion patterns predicted by DFT. Figure 4b shows the same MLFF phonon dispersion as Figure 4a but compares it with Stillinger-Weber (referred in this section as SW-MoS₂ the parametrization on Ref.¹⁸) and with Inelastic X-Ray Scattering measurements⁴⁸ shown as the black dots. Both MLFF and Stillinger-Weber (SW) dispersion curves were obtained with the assistance of the Alamode package⁴⁹. The first thing to be noticed here is that, although MLFF had a similar accuracy to SW-MoS₂ for the acoustic branches when compared with experimental data, MLFF follows the experimental results for optical branches closer than SW-MoS₂. When studying the lattice dynamics of a given system, special attention must be paid to the Γ modes, as they can be determined experimentally by IR and Raman measurements. Table 1 shows the predicted values for the four modes at Γ , comparing it with SW-MoS₂ and experimental results, each mode being drawn in Figure 5. It is worth mentioning that of all the modes, only E' and A_2'' are IR active, since their oscillation generates an instantaneous dipole moment and produces instantaneous polarization. All the modes are known to be Raman active except A_2'' , and both E' and A_1' being used widely in literature to characterize MoS₂ samples.

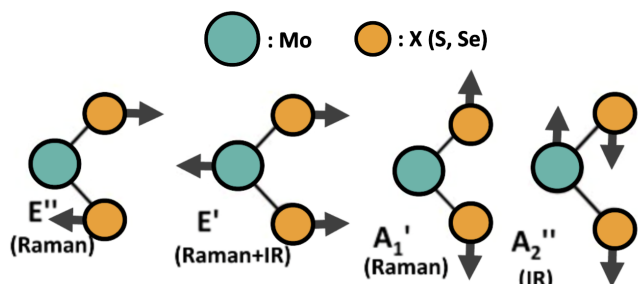


Figure 5 Sketch of the optical phonon modes of SL MoX_2 ($X = \text{S, Se}$) at Γ . Mo and X atoms were colored with turquoise and orange respectively.

Mode	MLFF	SW-MoS ₂	Exp. Results
E''	291.5	267.3	286 ³
E'	372.3	360.5	384.3 ¹ , 384.0 ² , 383 ³ , 383.7 ⁵
A_1'	390.8	429.2	403.1 ¹ , 408 ³
A_2''	459.0	506.8	470.0 ² , 466 ⁴ , 468.2 ⁵

¹ Ref. ⁵⁰ ² Ref. ⁵¹ ³ Ref. ⁴⁸ ⁴ Ref. ⁵² ⁵ Ref. ⁵³

Table 1 Phonon modes at Γ of SL-MoS₂. The unit is (cm^{-1})

3.1.2 THz dielectric spectra

Figure 6 shows the MD results for the dielectric spectra for MoS₂ at 300K at THz frequencies (from 100 cm^{-1} to 600 cm^{-1}). The spectra are divided into two parts: in-plane (considering only the components of the dipole moment that are parallel to the layer) and out-of-plane (considering only the component of dipole moment that is perpendicular to the layer), represented by the blue and red curves respectively. Figure 6b has two narrow absorption peaks, hence by fitting each peak to a Lorentzian oscillator²¹, the peak positions were calculated to be at $368.3 \pm 0.1 \text{ cm}^{-1}$ and $452.8 \pm 0.3 \text{ cm}^{-1}$ respectively. Figure 5 shows that the eigenvectors of the E' mode only alter the dipole moment in the planar directions while eigenvectors of the A_2'' only alter the dipole moment in the perpendicular ones. Thus, the peak illustrated by the blue curve can be compared to the E' value in Table 1 while the peak denoted by the red curve can be compared with A_2'' . Its noteworthy the proximity of the calculated values in Figure 6b and Table 1, with the presented redshift being attributed to temperature effects of the MD simulation. We can compare our simulation results with IR reflectivity measurements by Wieting *et. al.*⁵⁴ (more specifically with Figure 6 of the paper). The same narrow peak found in our simulations are present in the reflectivity measurements while their peak positions are located at 384 cm^{-1} for the in-plane mode and 472 cm^{-1} for the out-of-plane mode, being very close to the values obtained by the simulations using our MLFF.

Figure 7 shows our MD results for the THz dielectric spectra of MoS₂ obtained with the MLFF at 150 K, 350 K and 550 K. From it, we can discern several trends: with increasing temperature, both peaks in Figure 7 c,d broaden and redshift, a behavior in accordance with experiments⁵⁵. Figure 8 shows the temperature dependence of the E' and A_2'' modes based on the peak positions of the imaginary part of the spectra. The numerical values

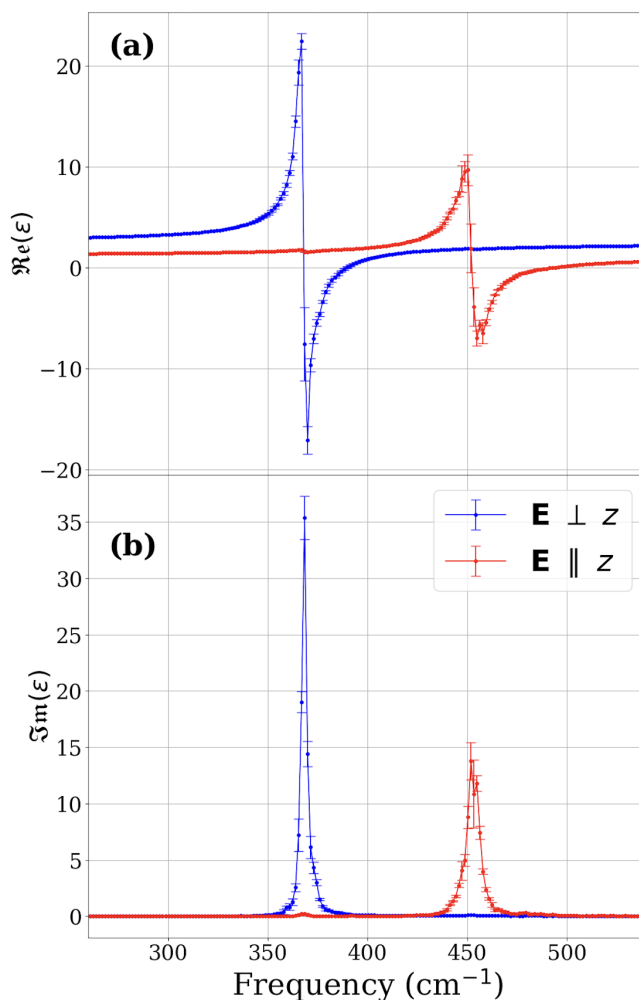


Figure 6 Real (a) and imaginary (b) part of the dielectric function for MoS₂ as a result of our MD simulations at 300K.

were obtained by fitting Lorentzian oscillators to the peaks presented in the data. To obtain the SW-MoS₂ data points, the same simulation procedure described in Sec. 2.3 was applied. Both simulations with MLFF and SW-MoS₂ produced a redshift with increasing of temperature. For each mode and for each potential, we performed linear fits (represented by dashed lines) and extracted the slope, which contains information about the average redshift of the system due to temperature. Table 2 shows results for the slopes and compares it to experimental results, indicating that our calculations are consistent with literature. Figure 9 shows our MD results for the THz dielectric spectra for MoS₂ obtained with the MLFF at 300 K using a unstrained lattice (0.0%), a lattice with 0.8% strain of the original and a lattice with 1.8% strain of the original. Qualitatively, the frequency peaks in Figure 9(c,d) become redshifted with the application of strain, similarly to the reported temperature effects. However, for more strained lattices the peaks are narrower than for unstrained ones. The redshift can be attributed to the weakening of the bonds caused by the tensile strain⁵⁶ while the narrowing of the peaks can be attributed to the fact that in a strained lattice, acoustic modes do not propagate as freely as in an unstrained lattice and, therefore,

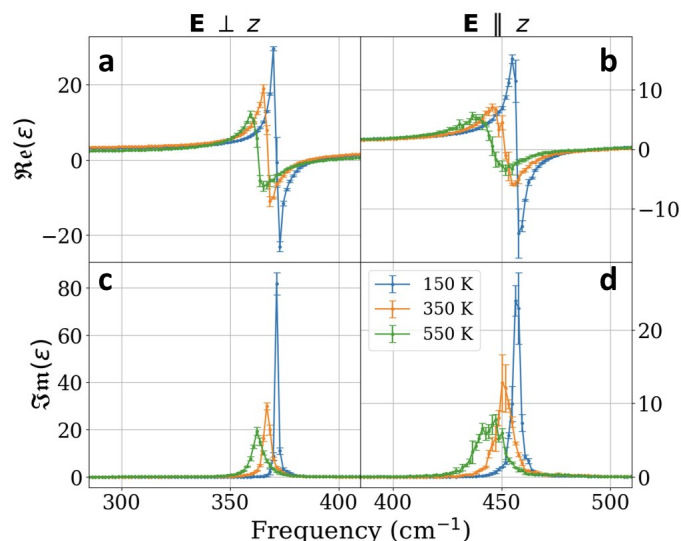


Figure 7 THz dielectric spectra for MoS₂ at 150 K, 350 K and 550 K. Results in Figure 8 for E' and A₂' modes are related to the peaks in (c) and (d) respectively. We included fewer temperatures than in Figure 8 for clarity.

cannot interfere with the propagation of optical modes. Figure 10 shows the strain dependence of the of the E' and A₂' modes. Similar to Figure 8, we performed linear fits and extracted the slope for each mode and for each potential. Table 3 shows the results for the temperature coefficients and compares it to experimental and other theoretical results. We notice a qualitative difference between the behavior of the A₂' mode for simulations with MLFF and SW-MoS₂, the latter presenting a slight blueshift with the application of strain, a result significantly different from the DFT prediction. For both modes, The MLFF reproduces DFT results more closely than SW-MoS₂. when comparing with experimental results, both potentials had similar performance for the E' mode. However, the diverse range of results for the E' mode prevents us

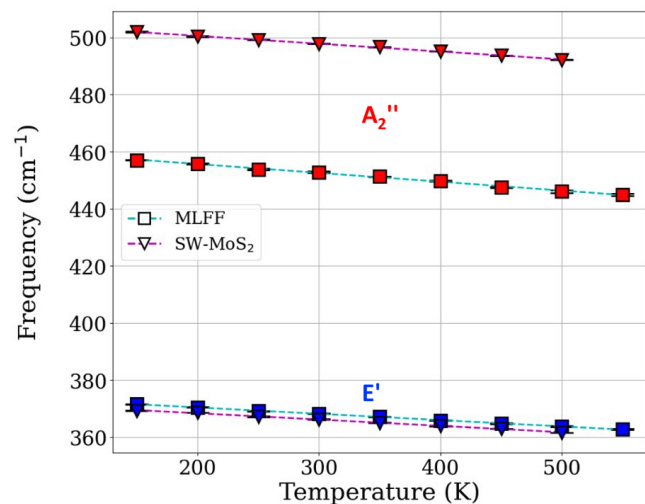


Figure 8 Temperature dependence of IR-active modes at MoS₂ for MLFF and SW-MoS₂ with error bars. Dashed lines indicates the linear fit performed to obtain the coefficients at Table 2.

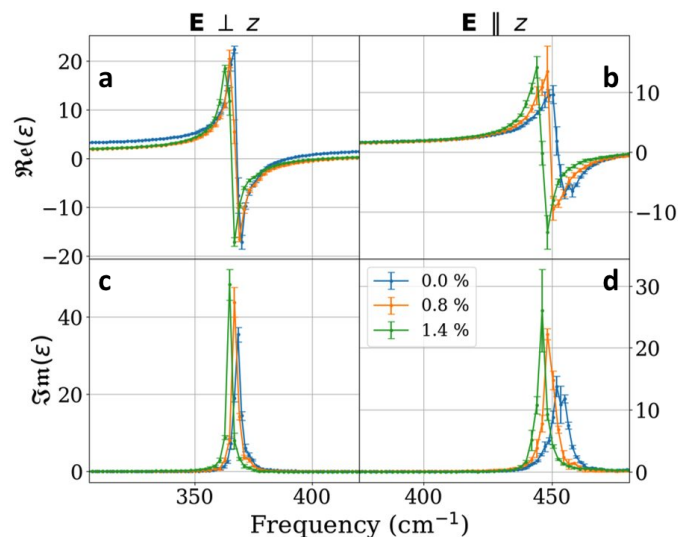


Figure 9 THz dielectric spectra for MoS₂ at 300 K for the strain percentages 0.0%, 0.8% and 1.4%. Results in Figure 10 for E' and A₂' modes are related to the peaks in (c) and (d) respectively. We included fewer strains than in Figure 10 for the sake of clarity.

from making any claims about the accuracy of our calculations regarding the temperature coefficient. Moreover, since the A₂' mode is not Raman active, to our knowledge, there are not any experimental results that studies the variation of that mode with strain. In that sense, our results are a prediction of the A₂' mode redshift including temperature effects.

3.2 MoSe₂

3.2.1 Phonon properties

Figure 11 shows the results for the phonon dispersion calculated with the developed MLFF for MoSe₂ in this study. The purpose for the comparison with DFT had already been described in Sec. 3.1.1 but, to our knowledge, there are not any experimental re-

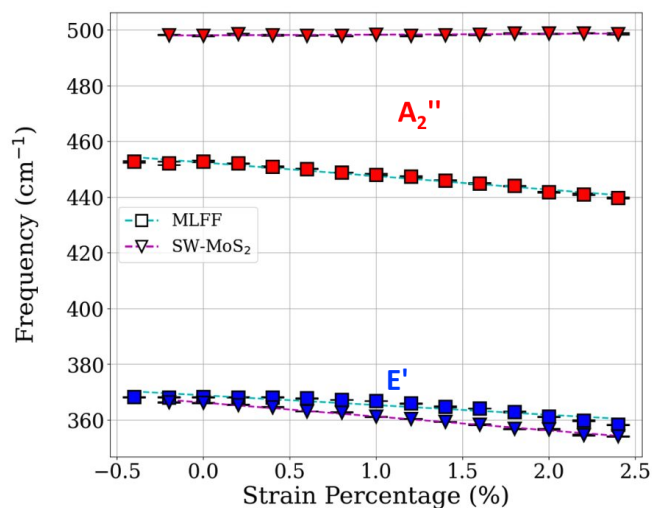


Figure 10 Strain dependence of IR-active phonon modes at MoS₂ for MLFF and SW-MoS₂ with error bars. Dashed lines indicates the linear fit performed to obtain the coefficients at Table 3.

Mode	MLFF	SW-MoS ₂	Exp. Results			
E'	-2.2	-2.2	-1.32 ¹ , -1.47 ² , -1.41 ³ , -1.79 ⁴ , -1.61 ⁵ , -1.36 ⁶ , -1.6 ⁷ , -1.3 ⁸			
A ₂ '	-3.1	-2.7	-1.99 ⁵			

¹ Ref. ⁵⁵ ² Ref. ⁵⁷ ³ Ref. ⁵⁸ ⁴ Ref. ⁵⁹ ⁵ Ref. ⁶⁰ ⁶ Ref. ⁶¹ ⁷ Ref. ⁶²
⁸ Ref. ⁶³

Table 2 Temperature coefficient for E' and A₂' modes of MoS₂ (10⁻² cm⁻¹/K).

Mode	MLFF	SW-MoS ₂	Exp. Results		DFT
E'	-3.49	-4.98	-7.4 ^{1a} , -3.2 ^{1b} , -4.5 ² , -2.1 ³ , -4.67 ⁴		-4.28 ⁵
A ₂ '	-4.87	0.26			-4.19 ⁵

^{1a,b} Ref. ⁶⁴ ² Ref. ⁶⁵ ³ Ref. ⁶⁶ ⁴ Ref. ⁶⁷ ⁵ Ref. ⁶⁸

^{1a} Spin Coated PVA encapsulation

^{1b} Conventional exfoliation

Table 3 Strain coefficient for E' and A₂' modes of MoS₂ (cm⁻¹/%).

sults in the literature on the modes for MoSe₂ at several points in the Brillouin zone (such as in Ref. ⁴⁸). We compare our results with Stillinger-Weber (referred in this section as SW-MoSe₂) as described in the parametrization proposed by Kandemir *et. al.*⁶⁹. For the optical phonon branches, we observe that the MLFF fits the DFT dispersion more closely than SW-MoSe₂ as expected. Table 4 shows the MLFF predicted values for the four modes at Γ , comparing it to SW-MoSe₂ and experimental results. From Table 4 we observe that SW-MoSe₂ predicts frequencies that are considerably redshifted when compared to experiment and that the MLFF predicts more accurate values. It is worth mentioning that the E' mode has a lower frequency than the A₁' mode in MoS₂ while the opposite is observed in MoSe₂.

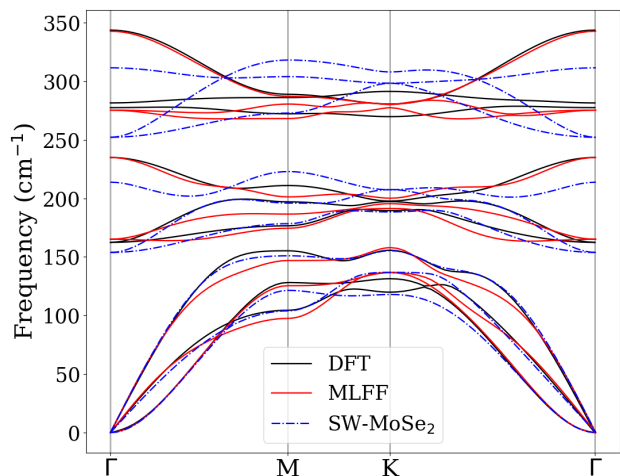


Figure 11 Phonon Dispersion for MoSe₂ along high symmetry directions Γ -M-K- Γ for the adjusted MLFF, DFT calculations and Stillinger-Weber (SW-MoSe₂) potential.

Mode	MLFF	SW-MoSe ₂	Exp. Results		
E''	165.1	153.8	168 ¹ , 170 ² , 175.8 ⁶		
A ₁ '	234.9	213.8	242 ¹ , 243 ² , 241.2 ³		
E	275.3	252.2	286.9 ⁴ , 289 ¹ , 287.3 ³ , 288 ⁵ , 286 ⁶ , 283 ⁷		
A ₂ '	342.7	311.5	352 ¹ , 350 ⁵ , 352 ⁶		

¹ Ref. ⁷⁰ ² Ref. ⁷¹ ³ Ref. ⁷² ⁴ Ref. ⁷³ ⁵ Ref. ⁷⁴ ⁶ Ref. ⁷⁵ ⁷ Ref. ⁷⁶

Table 4 Phonon modes at Γ of SL-MoSe₂. The unit is (cm⁻¹)

Mode	MLFF	SW-MoSe ₂	Exp. Results		
E'	-0.79	-3.9	-1.18 ¹ , -1.21 ² , -0.69 ³		
A ₂ '	-2.1	-3.7	-0.64 ³ , -0.86 ⁴		

¹ Ref. ⁷⁷ ² Ref. ⁵⁸ ³ Ref. ⁷⁸ ⁴ Ref. ⁷⁹

Table 5 Temperature coefficient for E' and A₂' modes of MoSe₂ (10⁻² cm⁻¹/K).

Mode	MLFF	SW-MoSe ₂	Exp. Results	DFT
E'	-0.95	-1.59	-4.93 ¹	-4.28 ²
A ₂ '	-2.54	-5.6		

¹ Ref. ⁸⁰ ² Ref. ⁸¹

Table 6 Strain coefficient for E' and A₂' modes of MoSe₂ (cm⁻¹/%).

3.2.2 THz dielectric spectra

Figure 12 shows the MD results for the MoSe₂ THz dielectric spectra at long wavelengths similar to Figure 6 in Sec. 3.1.1. In Figure 12b, the peak for the blue and red curves respectively are localized at 269.8 ± 0.1 cm⁻¹ and 334.9 ± 0.1 cm⁻¹ respectively, which can be compared directly with the values from Table 4 for the E' and A₂' for the same reasons given before. Similar to what was observed on MoS₂, we can assign those modes to the peaks, and the difference of the peak positions and the tabled values also can be attributed to a redshift effect due to temperature in our simulations. We can compare our results to infrared reflectance results from Sekine *et. al.*⁷⁰ (see Figure 6 of the referred work), as they assigned the values 289 cm⁻¹ and 352 cm⁻¹ to the modes E' and A₂' respectively. Figure 13 shows our MD results for the THz dielectric spectra of MoSe₂ obtained with the MLFF at 150 K, 300 K and 450 K. The same qualitative trends observed on our MLFF simulations for MoS₂ can be observed on MoSe₂, i.e., the redshift and broadening of the peaks in Figure 13 c,d. However, the broadening is less pronounced than those in Figure 7 c,d. Figure 14 and Table 5 shows our results for the temperature dependence of the infrared active phonon modes, comparing it with simulations with SW-MoSe₂ and experimental results. We notice that, when comparing with experiments, the simulations with our MLFF predicts more accurate coefficients than SW-MoSe₂ and, although the MLFF prediction for the temperature coefficient of the A₂' mode is considerably different than the experimental values, it is still a better prediction than those given by SW-MoSe₂. Also, SW-MoSe₂ predicts similar temperature coefficients for the two distinct modes while in the MLFF simulations the temperature coefficient seems to be sensitive to the oscillation mode. Figure 15 shows results for the THz dielectric spectra of MoSe₂ at 300 K for the unstrained lattice (0.0%), and lattices with 0.8% and

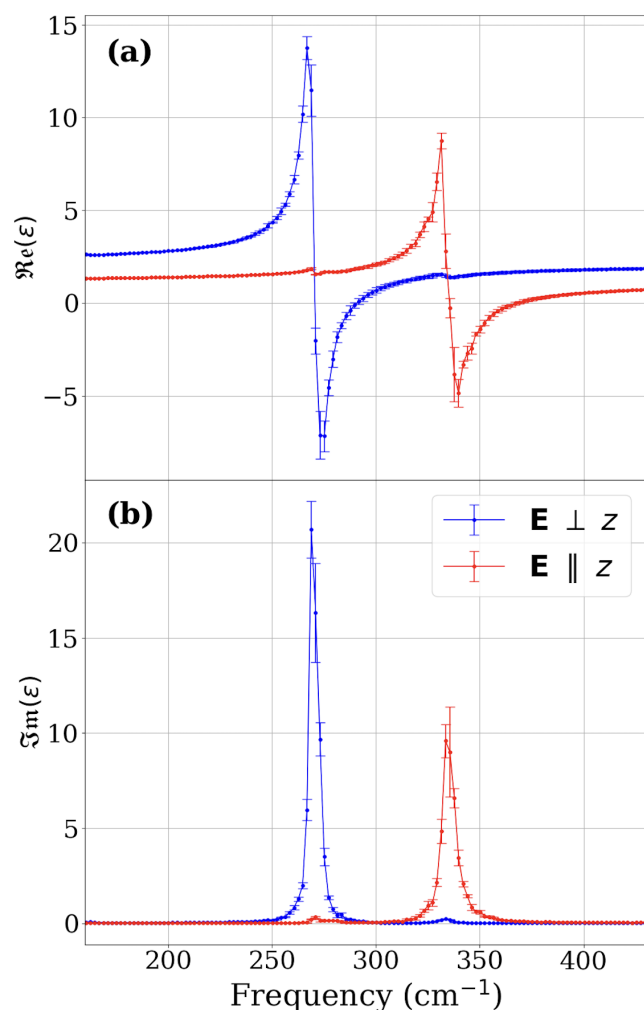


Figure 12 Real (a) and imaginary (b) part of the dielectric function for MoSe_2 as a result of our MD simulations at 300K.

1.8% strain respectively. Although a redshift of the peak is noticed, we did not observe any noticeable changes on the breadth of the peaks. Figure 16 and Table 6 shows our results for the strain dependence of the infrared active phonon modes. The lack of other reported experimental or theoretical results made it difficult to rate the performance our MLFF. To our knowledge, the references cited at Table 6 were the only studies that reported the strain coefficients for the E' mode and there are no reports for the A_2'' mode. When comparing to these reported data, neither our MLFF nor SW-MoSe₂ presented accurate results.

3.3 Rippling Effects

Figure 17 illustrates the imaginary part of the dielectric spectra for both systems (akin to Figures 6(b) and 12(b)), but specifically focusing on regions with low absorption intensities, with a version of the same data plotted on a semi-log scale that is included in Figure S7 in Sec. 4.3 of ESI†. Within the figure, it is evident that each system exhibits four distinct new peaks. Noticeably, two of these peaks align precisely with the frequencies of the E' and A_2'' modes, however with reversed polarization directions. Addi-

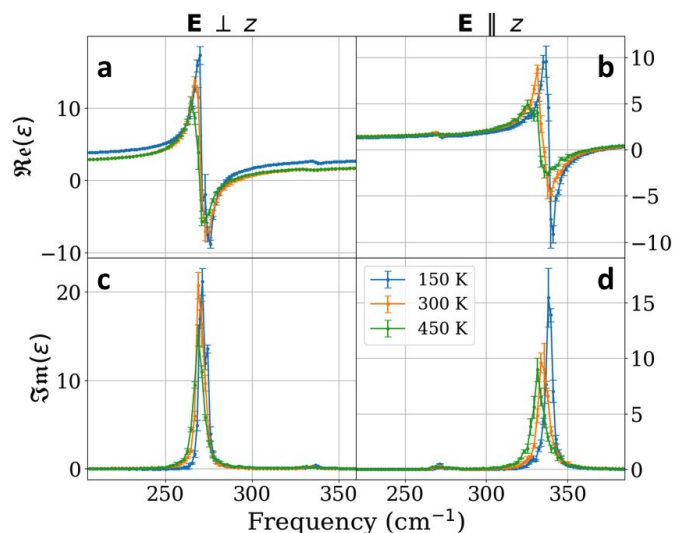


Figure 13 THz dielectric spectra for MoSe_2 at 150K, 300K and 450K. Results in Figure 14 for E' and A_2'' modes are related to the peaks in (c) and (d) respectively. We included fewer temperatures than in Figure 14 for the sake of clarity.

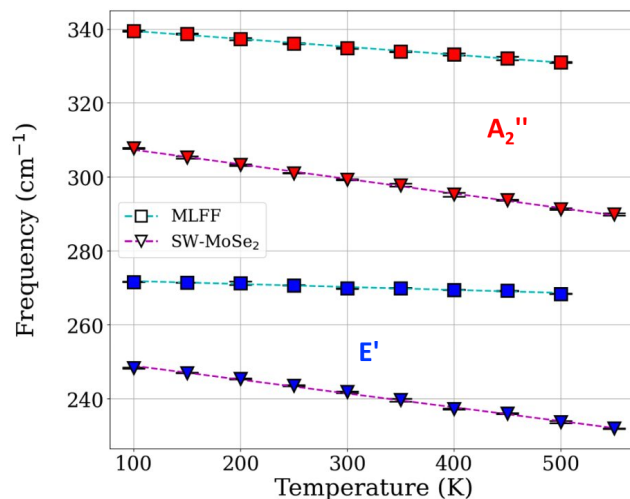


Figure 14 Temperature dependence of IR-active phonon modes in MoSe_2 for MLFF and SW-MoSe₂. Dashed lines indicates the linear fit performed to obtain the coefficients in Table 5.

tionally, MoS_2 displays peaks at approximately 310 cm^{-1} and 393 cm^{-1} , whereas MoSe_2 features peaks around 163 cm^{-1} and 225 cm^{-1} , values closely matching the frequencies of the E'' and A_1' modes as listed in Tables 1 and 4, respectively. Observing these new peaks allows us to identify two key characteristics in our simulations. Firstly, the E' and A_2'' modes exhibit infrared (IR) activity in a direction perpendicular to their usual oscillation. Secondly, there is a manifestation of some IR activity, although minimal, by the E'' and A_1' modes, traditionally considered IR inactive. Moreover, we noticed that all of the newly observed peaks were extinguished under the application of tensile strain (see Figure S8 in ESI†).

Applying strain to the lattice reduces fluctuations in its height, thereby diminishing the amplitude of ripples, as depicted in Fig-

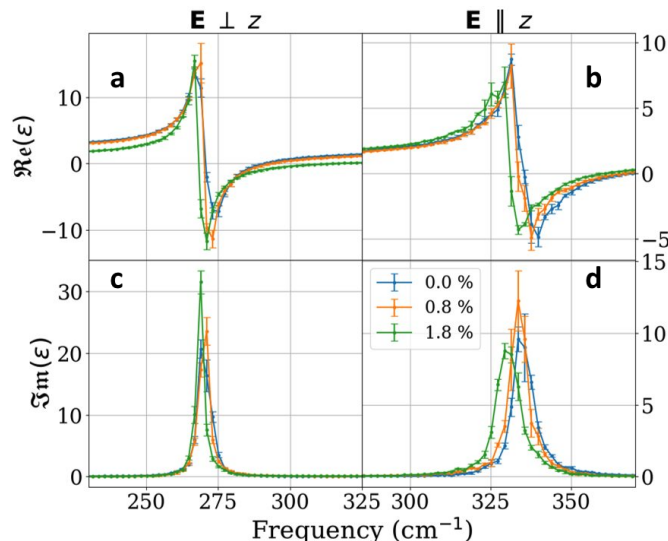


Figure 15 THz dielectric spectra for MoSe₂ for the strain percentages 0.0%, 0.8% and 1.4%. Results in Figure 16 for E' and A₂' modes are related to the peaks in (c) and (d) respectively. We included fewer temperatures than in Figure 16 for the sake of clarity.

ure 18. This figure demonstrates that in both systems, the average height (defined as the difference in the z coordinate between the highest and lowest Mo atom, as illustrated in the figure) decreases with increasing strain. For MoS₂ the average height decreases from 9Å to 2Å while for MoSe₂ it decreases from 6Å to 2Å when a strain 2% above the equilibrium lattice constant is applied. Therefore, considering the data presented in Figures 17 and 18, it can be inferred that the observed low-intensity peaks observed correlate with the ripples present in SL-MoS₂ and MoSe₂. In the vicinity of the peaks corresponding to the frequencies adjacent to the E' and A₂' modes, the mechanism by which ripples induce IR activity with altered polarizations becomes clearer. By allowing the lattice to ripple, the E' mode is no longer confined strictly to

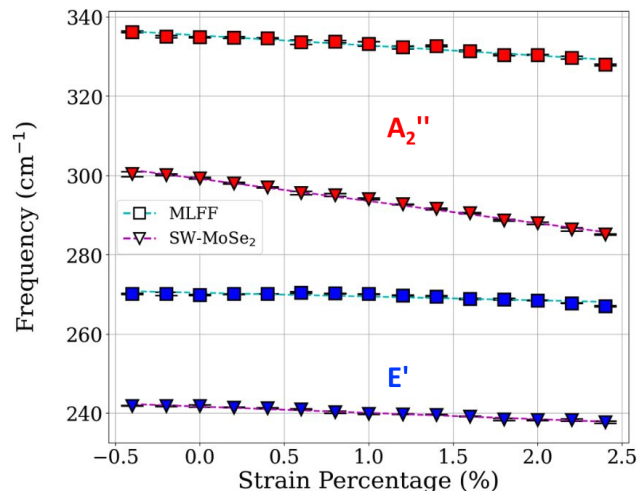


Figure 16 Strain dependence of IR-active phonon modes at MoSe₂ for MLFF and SW-MoSe₂. Dashed lines indicates the linear fit performed to obtain the coefficients at Table 6.

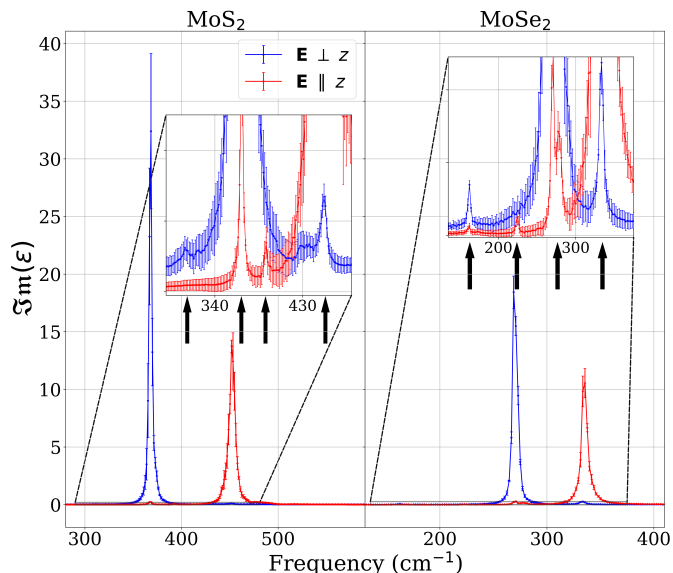


Figure 17 Imaginary part of dielectric spectra for MoS₂ and MoSe₂ at 300K with insets in the small intensities region. Arrows indicate peaks centered at 310(163), 368(225), 393(271) and 452(334) for MoS₂ (MoSe₂) in cm⁻¹.

the plane, and similarly, the A₂' mode is not restricted solely to the axis perpendicular to the plane. This results in the E' mode acquiring an out-of-plane component and the A₂' mode acquiring a planar component, as depicted in Figure 19. However, this explanation alone does not suffice to elucidate the observed IR activity near the frequencies associated with the E'' and A₁' modes in our simulations. To gain further insight into the influence of ripples on the dielectric spectra and to explore potential explanations for the peaks observed at E'' and A₁', we constructed a supercell composed of 1020 atoms. Within this supercell, we introduced a sinusoidal wave characterized by a wave vector \mathbf{k} parallel to the \hat{x} -axis, with a wavelength determined by the total length of the cell in the x -direction. This supercell is depicted in Figure S9 of the ESI† and maintains translational symmetry along the y direction and this simplified model for the ripple was used to qualitatively investigate the origins of the new peaks observed in the spectra. Using the MLFFs to model atomic interactions, we employed the Alamo package to compute the phonons of the primitive cell (see Figure S10 at ESI†) corresponding to the rippled supercell at the Γ point. The calculations also provided the eigenvectors $\mathbf{U}_j(\kappa)$ associated with each frequency eigenmode ω_j . These eigenvectors enable the determination of the IR intensities for each mode, calculated using the equations defined in Eqs. 2.112 and 2.114 of Ref.⁸²:

$$f(\omega_j) = \sum_{\beta=x,y,z} \left| \sum_{\kappa=1}^{N_{at}} \frac{e_{\kappa}}{\sqrt{M_{\kappa}}} U_j(\kappa, \beta) \right|^2 \quad (3)$$

where e_{κ} and M_{κ} denote the charge and mass of atom κ , respectively†. An oscillation mode j contributes to $\text{Im}[\epsilon(\omega)]$ only if $f(\omega_j)$

† The index κ denotes the atom within the unit cell. The vector $\mathbf{U}_j(\kappa)$ can be ex-

is non-zero, serving as a selection rule for IR absorption^{83,84}. Consequently, it becomes feasible to attribute each peak in Figure 17 to those specific oscillation modes with non-zero $f(\omega_j)$.

The IR intensities results for MoS₂ and MoSe₂ are shown in Figures 20 and 21, respectively and the calculated frequencies for all modes are listed in Tables S1 and S2 in ESI†. In each, the calculation for the unrippled (flat) cell was included at Figures 20a) and 21a) for comparison purposes and the insets were included to facilitate visualization of all modes with low intensity $f(\omega_j)$. As expected for the flat cell in both compounds, only the E' and A₂' modes showed a non-zero IR response. The E' mode presents an in-plane response only while the A₂' mode presents an out-of-plane response only. For the rippled cell, a degeneracy breaking in frequencies is observed due to the breaking of some symmetries of the system caused by the introduction of the ripple. This symmetry breaking causes the only two modes present in the flat cell to split into several bars located at frequencies close to the E' and A₂' modes in the flat cell. However, it is still expected that the new modes introduced by the ripple must have some similarity to those of the original cell due to the fact that they share similar frequencies. In both compounds the two largest bars, one blue and one red, correspond to the vibrations that best represent the E' and A₂' modes of the flat cell in the rippled cell, the characteristic vibration of the E' in the planar directions and the characteristic vibration of the A₂' in the out-of-plane direction. These bars would correspond to the main peaks depicted in Figures 6b) and 12b). Looking at the low IR intensity modes, it is noticeable that in both Figures 20b) and 21b) the presence of a mode with a frequency close to E' that presents out-of-plane IR activity (indicated by the red bar) as well as a mode with a frequency close to A₂' that presents in-plane IR activity (indicated by the blue bar) in both figures. Furthermore, both figures indicate the presence of modes with IR activity at frequencies close to those of the E'' and A₁' modes which, in the flat cell, are known to be IR inactive. Thus, the degeneracy breaking caused by the introduction of the ripple is also responsible for the splitting of the E'' and A₁' modes into several modes, some of which have some IR activity. The

pressed in terms of the Cartesian unit vectors \hat{x} , \hat{y} , and \hat{z} as $\mathbf{U}_j(\kappa) = U_j(\kappa, x)\hat{x} + U_j(\kappa, y)\hat{y} + U_j(\kappa, z)\hat{z}$. The components referenced in Eq. 3 are defined accordingly in this footnote.

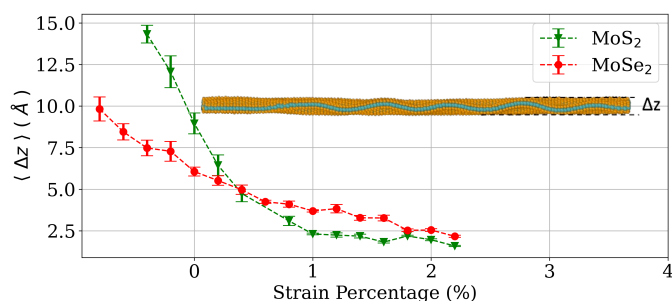


Figure 18 Mean lattice height as function of strain for MoS₂ and MoSe₂ during a simulation. The sketch of the rippled single-layer serves to outline the definition of the height Δz of the lattice.

results shown in Figures 20 and 21 strengths the hypothesis that lattice ripples would be responsible for the appearance of new peaks present in the simulations and shown in Figures 17.

The main advantage of calculating the eigenvectors of the ripples lattice lies in the ability to observe the patterns of new vibrational modes and understand how these modes affect the total electric dipole moment of the cell, which will be shown on the following figures. Here, we denote the modes of the rippled cell with the same notation of Tables 1 and 4 to indicate the mode of the flat cell that generated the new mode, but we will use a "*" to indicate that this mode belongs to the rippled cell and we will indicate the direction of polarization of the mode in parenthesis. Figure 22 shows the modes *E'(z) and *A₂'(x), found to have IR activity next to E' and A₂' with inverted polarizations at Figures 20(b-ii, iv) and 21(b-iii, iv). Upon comparing the modes depicted in Figures 5 and 22, a discernible similarity emerges between modes *E'(z) and *A₂'(x) in relation to modes E' and A₂' respectively. This similarity arises due to certain MoS(Se)₂ units within the rippled supercell exhibiting identical vibrational pattern as those observed in the primitive flat cell, leading to similar oscillation frequencies in these modes. However, Figure 22 reveals how the oscillation of the whole rippled cell lead to alterations in its total dipole and in which direction. In mode *E'(z), the cell exhibits a oscillation pattern resembling E', with atoms on either side of the ripple crest moving in opposite directions, which results in the cancellation of the horizontal component of total dipole moment of the mode, leaving only a resultant vertical component. Thus, mode *E'(z) manifests an out-of-plane infrared (IR) response with a frequency close to E', consistent with the results shown in Figure 17. Similarly, in mode *A₂'(x), the cell displays an oscillation pattern akin to A₂', also with atoms on either side of the ripple crest moving oppositely similar to *E'(z). This leads to the cancellation of the vertical component, leaving predominantly only a resultant horizontal component. Consequently, mode *A₂'(x) exhibits an in-plane IR response with a frequency close to A₂', which is also consistent with the results in Figure 17. The analysis of modes *E'(z) and *A₂'(x) on Figure 22 strengths the hypothesis depicted in Figure 19, wherein the rip-

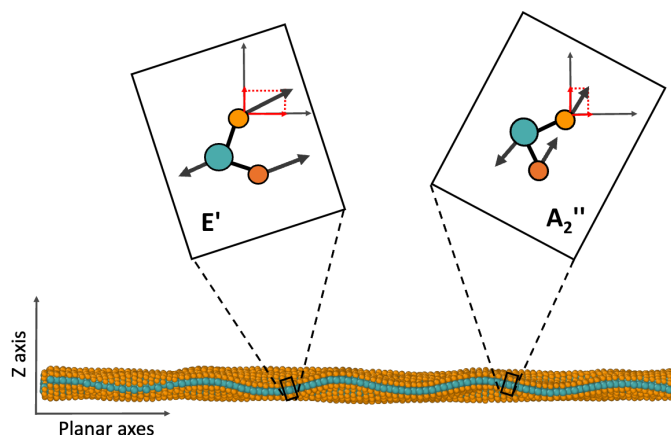


Figure 19 Sketch of the decomposition of the components of the oscillation modes E' and A₂' in a rippled lattice.

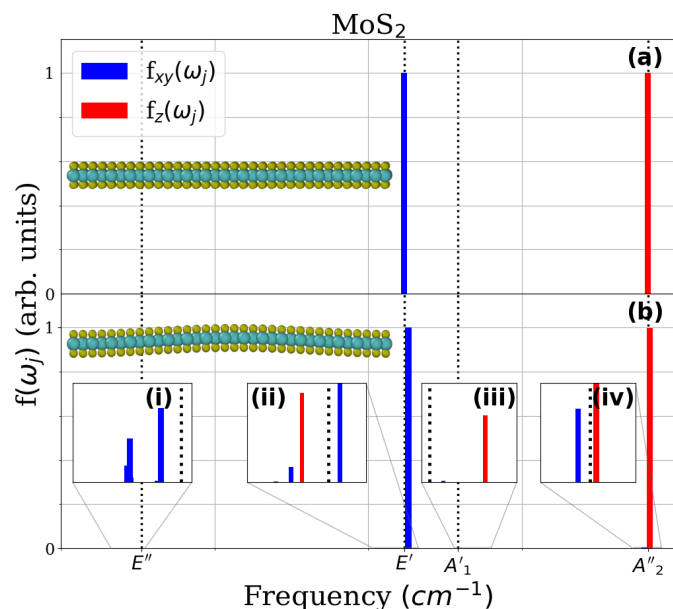


Figure 20 IR intensities for the MoS₂. (a) and (b) indicate the calculated intensities for the cell without and with the ripple, respectively. The dotted lines represent the frequencies listed in Table 1.

pled lattice causes modes E' and A_2'' to acquire out-of-plane and in-plane components, respectively. Figure 23 shows the modes $*E''(x)$ and $*E''(y)$ related to the two highest blue bars at Figure 20(b-i) for MoS₂ and Figure 21(b-i) for MoSe₂, both of them presenting IR activity next to E'' . These modes exhibit an oscillation pattern similar to E'' , where atoms on opposite sides of the crest move in opposite directions. However, both modes appear to curve next to the ripple, with the $*E''(x)$ curving horizontally and the $*E''(y)$ curving vertically. Thus, the oscillation pattern depicted in Figure 23, as predicted by the MLFFs, suggests that the ripple induces curvature in the displacement vector fields of S(Se) atoms, particularly near its inflection point. This curvature, visible on the top view of the sketch of both modes, is responsible for the emergence of a dipole moment perpendicular to the axis along which the atoms predominantly move. In the $*E''(x)$ mode, for instance, S(Se) atoms primarily move in the y direction and the curvature introduces a component of the displacement patterns in the x direction while in the $*E''(y)$ mode, the atoms primarily move in the x direction and the curvature is responsible for the component in the y direction. Therefore, the dipole moment component on the primary axis of movement of the atoms is

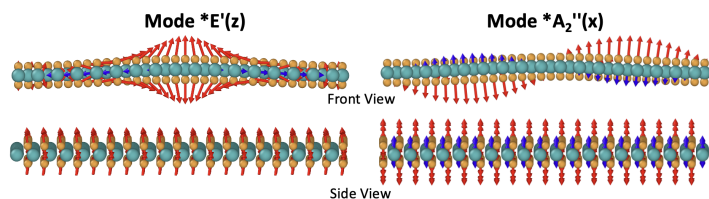


Figure 22 Sketch of the oscillation patterns of the modes $*E'(z)$ and $*A_2''(x)$ in the rippled cell. The directions of displacements of the Mo and S(Se) atoms are indicated by blue and red vectors respectively.

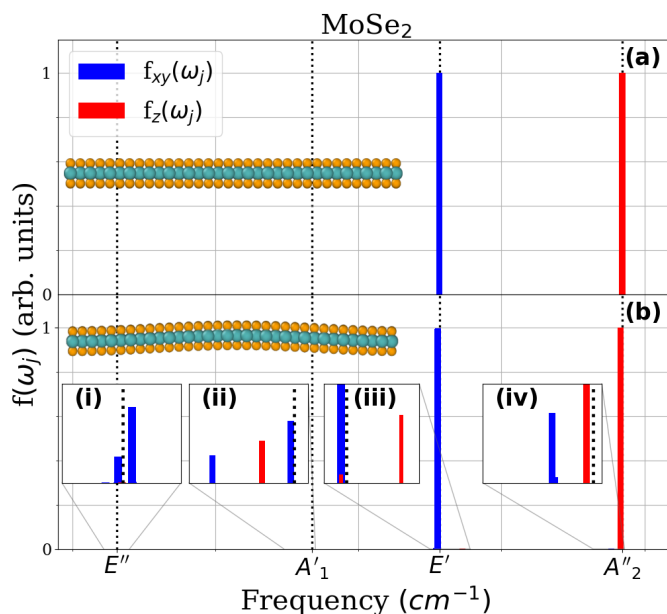


Figure 21 IR intensities for the MoSe₂. (a) and (b) indicate the calculated intensities for the cell without and with the ripple, respectively. The dotted lines represent the frequencies listed in Table 4.

anceled, and the resultant component on its perpendicular axis is due to curvature induced by the ripple. The emergence of a resultant dipole moment of the cell is apparent on the front view of the $*E''(x)$ mode, with all arrows slightly pointing to the right, and on the side view of the $*E''(y)$, with all arrows slightly pointing to the right and other modes with similar displacement patterns but with atoms on opposite sides of the crest move in the direction were found to have no IR activity. Our results for the eigenmodes suggest that this mechanism described for the $*E''(x)$ and $*E''(y)$ modes is consistent with the appearance of the peaks close to the E'' frequency at Figure 17 and provides a feasible explanation for them. Figure 24 illustrates mode $*A_1'(z)$ associated with the red bars in Figure 20(b-iii) for MoS₂ and Figure 21(b-ii) for MoSe₂, indicating their IR activity near A_1' . Displacement vectors are color-coded according to maximum displacement along the z -axis over half oscillation period, with red indicating greater displacement. This mode exhibit an oscillation pattern similar to A_1' , with the Mo-layer remaining stationary while the top and bottom S(Se)-layers moving symmetrically. However, upon examining the color of the displacement vectors, it is evident that the bottom layer exhibits larger displacements on average compared to the top layer, resulting in a greater distance from the Mo-layer. This disparity in displacement between the layers can induce a slight modification in the total dipole moment of the cell, thereby generating the observed out-of-plane IR activity depicted in Figure 20(b-iii) for MoS₂ and Figure 21(b-ii) for MoSe₂. Our results for the eigenmodes suggest that this mechanism described for the $*A_1'(z)$ mode is consistent with the appearance of the peaks close to the A_1' frequency at Figure 17 and provides a feasible explanation for it. It is noteworthy that several modes exhibiting planar IR activity were identified near the E' mode in Figure 20(b-ii) and near the A_1' mode in Figure 21(b-ii). However, since the A_1'

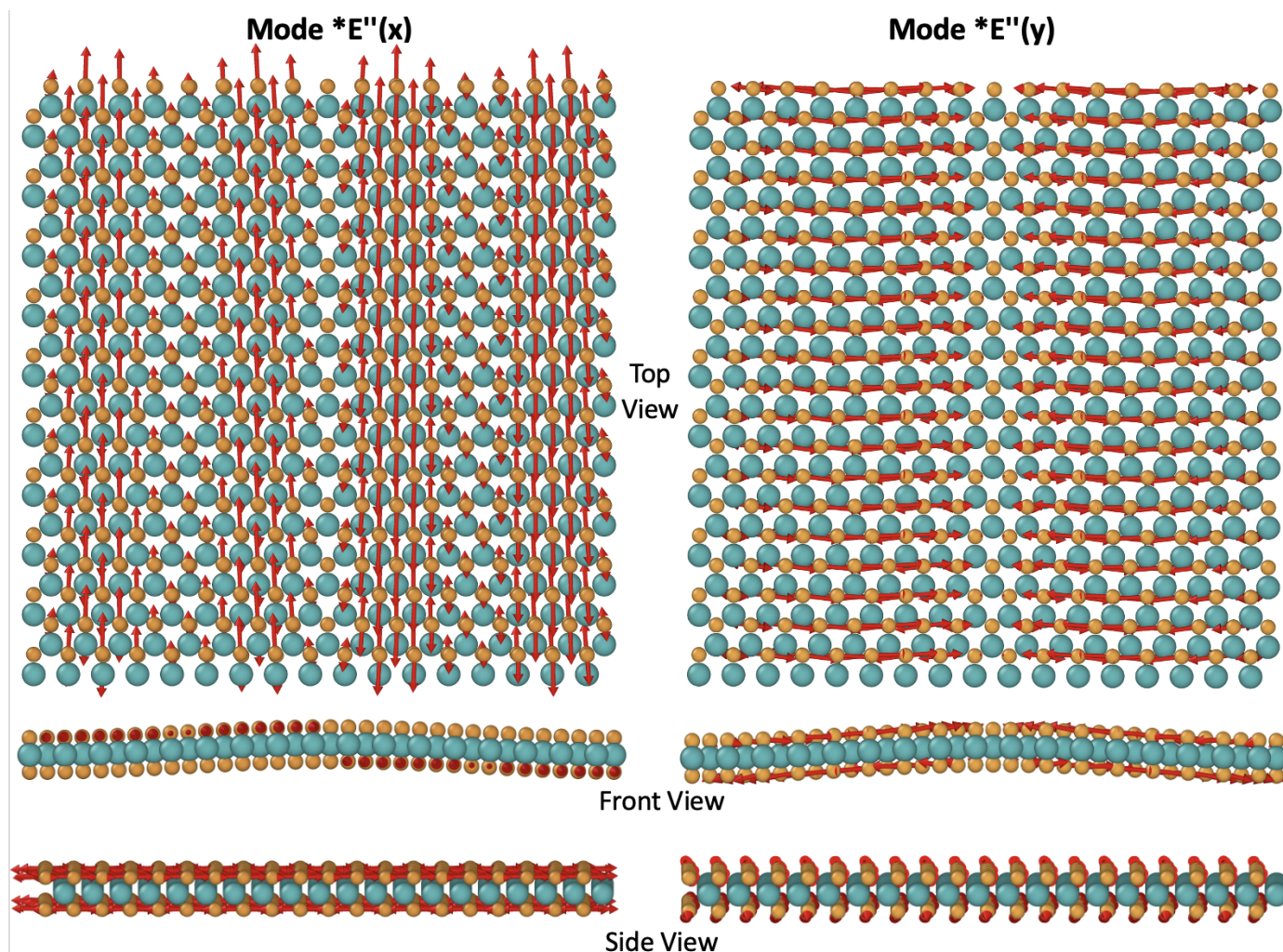


Figure 23 Sketch of the oscillation patterns of the modes $*E''(x)$ and $*E''(y)$ in the rippled cell. The directions of displacements of the S(Se) atoms are indicated by red vectors.

frequency is close to the E' in both compounds, we believe that these peaks were suppressed by the broadening of the E' mode main blue peak in our simulations as shown in Figure 17.

4 Conclusions

In this work, using machine learning, we developed two MLFFs for MoS_2 and MoSe_2 that captures their main dynamical properties. We tested its validity by calculating its phonon dispersion and making an accurate correspondence between the structures included in the reference data set and the modes desired to model on MD simulations. With that procedure, we were able to reproduce known experimental dielectric spectra at THz frequencies. To test the performance of the force fields generated in this work, we focused on reproducing results for the peak-frequencies and their redshift due to temperature and strain, comparing it with well known Stillinger-Weber parametrizations of the respective materials. In general, the phonon dispersion obtained using our MLFF were more accurate than Stillinger-Weber as well the MD results for the IR-active phonon frequencies. For the temperature coefficient, MLFF and SW presented similar capability of recreating experimental results for MoS_2 while for MoSe_2 the MLFF

has a better performance. For the MoS_2 strain coefficient, SW predicted that the A_2'' mode shows a blueshift, which contradicts other ab initio results previously reported. Simulations with MLFF predicted a redshift for the strain coefficient of both infrared active modes, which is in accordance to previous experimental and ab initio results. Furthermore, our simulations reveal the appearance of new low-intensity peaks in the THz dielectric spectra, especially those in proximity to the IR-inactive frequencies E'' and A_1' . Molecular dynamics (MD) simulations investigating the

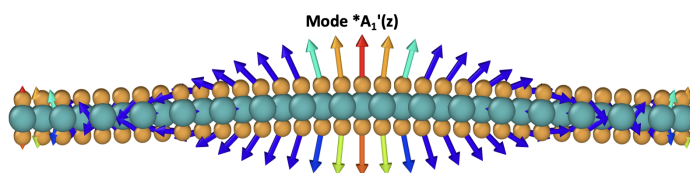


Figure 24 Sketch of the oscillation patterns of the mode $*A_1'(z)$ in the rippled cell. The directions of displacements along the z-axis of the S(Se) atoms are indicated by vectors and its colors shows the maximum displacement of each during the first half period of oscillation, with the scale increasing from blue to red.

height Δz of strained lattices establish a correlation between these emerging peaks and the propagation of thermal ripples, as evidenced by their significant reduction on lattices with smaller Δz . To explore potential explanations for the new observed peaks, we have calculated the eigenfrequencies and eigenmodes of a sine-rippled supercell with wave vector parallel to the zigzag direction using our MLFFs for each compound. The eigenmodes results for the frequencies next to E' and A_2'' with IR activities with inverted polarizations strengthens our initial hypothesis suggesting that permitting the layer to undulate frees the modes from oscillating exclusively along their original axis, enabling a component along the perpendicular axis. Moreover, the eigenmodes results for frequencies next to E'' suggests that, according the MLFFs modeled in this work, the ripples induces a curvature on the displacement vector field of the oscillation pattern and this curvature is responsible for the appearance of the peaks related to E'' on the spectra. The reasons for the appearance of such curvature on a rippled layer have not yet been discovered. Finally, the eigenmodes results for frequencies next to A_1' suggests that the resultant dipole moment at z is originated by the disparity of the distance of the top and the bottom layer with respect to the Mo-layer. These results may have far-reaching implications on the understanding of thermal ripples on 2D materials and, after testing the reliability and functionality of the MLFFs, they can be applied to study similar problems related to the phonon properties of MoS_2 and MoSe_2 . In future work, we plan to extend both MLFFs to study the role of defects, such as vacancies and dopants, on the layer dynamics⁸⁵.

Conflicts of interest

The authors declare no conflict of interest.

Data availability

All data supporting the conclusions of this study, including the MLFFs presented in this work, the database used for its development and animations for the discussed modes are available on the following Github repository: <https://github.com/gbsouza1997/TMD-MLFF-repo.git>.

Acknowledgements

This work received financial support from Conselho Nacional de Desenvolvimento Científico e Tecnológico - Brazil (CNPq) under grants CNPq 402091/2012-4, CNPq 163465/2021-5, Fundação de Amparo à Pesquisa do Estado de Minas Gerais - Brazil (FAPEMIG) under grants FAPEMIG RED-00458-16 and FAPEMIG APQ-01414-22, Coordenação de Aperfeiçoamento de Pessoal de Nível Superior - Brazil (CAPES) under grant CAPES 88887.840135/2023-00. G.B.G was also partially supported by the Simons Foundation and the Vice Provost for Graduate Education at The University of Georgia. S. B. H and Y. A. acknowledge support from the Air Force Office of Scientific Research (AFOSR) grant numbers FA9550-19-0252 and FA9550-23-1-0375. This study was supported in part by resources and technical expertise from the Georgia Advanced Computing Resource Center (GACRC), a partnership between the University of Georgia's Office of the Vice President for Research and Office of

the Vice President for Information Technology. G.B.G and V.B also thank Dr. Atanu Samanta from University of Pennsylvania (UPENN) for fruitful discussions.

References

- 1 A. Molina-Sánchez, K. Hummer and L. Wirtz, *Surf. Sci. Rep.*, 2015, **70**, 554–586.
- 2 M. Chhowalla, Z. Liu and H. Zhang, *Chem. Soc. Rev.*, 2015, **44**, 2584–2586.
- 3 K. F. Mak, C. Lee, J. Hone, J. Shan and T. F. Heinz, *Phys. Rev. Lett.*, 2010, **105**, 136805.
- 4 A. Ramasubramaniam, *Phys. Rev. B*, 2012, **86**, 115409.
- 5 V. K. Sangwan, H.-S. Lee, H. Bergeron, I. Balla, M. E. Beck, K.-S. Chen and M. C. Hersam, *Nature*, 2018, **554**, 500–504.
- 6 X. Wang and A. Tabarraei, *Appl. Phys. Lett.*, 2016, **108**, 191905.
- 7 M. M. Ugeda, A. J. Bradley, S.-F. Shi, F. H. Da Jornada, Y. Zhang, D. Y. Qiu, W. Ruan, S.-K. Mo, Z. Hussain, Z.-X. Shen *et al.*, *Nat. Mater.*, 2014, **13**, 1091–1095.
- 8 M. P. Allen and D. J. Tildesley, *Computer Simulation of Liquids*, Oxford University Press, 2017.
- 9 S. B. Hancock, D. P. Landau, N. A. Aghamiri and Y. Abate, *Phys. Rev. Mater.*, 2022, **6**, 076001.
- 10 D. C. Rapaport, *The Art of Molecular Dynamics Simulation*, Cambridge University Press, 2nd edn, 2004.
- 11 J. Tersoff, *Phys. Rev. B*, 1988, **37**, 6991–7000.
- 12 W. L. Jorgensen, J. Chandrasekhar, J. D. Madura, R. W. Impey and M. L. Klein, *J. Chem. Phys.*, 1983, **79**, 926–935.
- 13 D. Braun, S. Boresch and O. Steinhauser, *J. Chem. Phys.*, 2014, **140**, 064107.
- 14 P. Höchtel, S. Boresch, W. Bitomsky and O. Steinhauser, *J. Chem. Phys.*, 1998, **109**, 4927–4937.
- 15 P. Vashishta, R. K. Kalia, J. P. Rino and I. Ebbsjö, *Phys. Rev. B*, 1990, **41**, 12197–12209.
- 16 M. S. Daw and M. I. Baskes, *Phys. Rev. B*, 1984, **29**, 6443.
- 17 J.-W. Jiang, H. S. Park and T. Rabczuk, *J. Appl. Phys.*, 2013, **114**, 064307.
- 18 J.-W. Jiang, *Nanotechnology*, 2015, **26**, 315706.
- 19 A. Ostadhossein, A. Rahnamoun, Y. Wang, P. Zhao, S. Zhang, V. H. Crespi and A. C. T. van Duin, *J. Phys. Chem. Lett.*, 2017, **8**, 631–640.
- 20 O. T. Unke, S. Chmiela, H. E. Saucedo, M. Gastegger, I. Poltavsky, K. T. Schütt, A. Tkatchenko and K.-R. Müller, *Chem. Rev.*, 2021, **121**, 10142–10186.
- 21 M. Fox, *Optical Properties of Solids*, OUP Oxford, 2010.
- 22 G. Srivastava, *The Physics of Phonons*, Routledge, 1990.
- 23 N. D. Mermin, *Phys. Rev.*, 1968, **176**, 250–254.
- 24 D. Nelson, T. Piran and S. Weinberg, *Statistical Mechanics Of Membranes And Surfaces: 2nd Edition*, World Scientific Publishing Company, 2004.
- 25 A. Fasolino, J. Los and M. I. Katsnelson, *Nat. Mater.*, 2007, **6**, 858–861.
- 26 J. C. Meyer, A. K. Geim, M. I. Katsnelson, K. S. Novoselov, T. J. Booth and S. Roth, *Nature*, 2007, **446**, 60–63.

- 27 J. Brivio, D. T. L. Alexander and A. Kis, *Nano Lett.*, 2011, **11**, 5148–5153.
- 28 P. Anees, M. C. Valsakumar and B. K. Panigrahi, *Phys. Chem. Chem. Phys.*, 2017, **19**, 10518–10526.
- 29 S. Li, Y.-P. Wang, S. Ning, K. Xu, S. T. Pantelides, W. Zhou and J. Lin, *Nano Lett.*, 2023, **23**, 1298–1305.
- 30 P. Giannozzi, S. Baroni, N. Bonini, M. Calandra, R. Car, C. Cavazzoni, D. Ceresoli, G. L. Chiarotti, M. Cococcioni, I. Dabo, A. D. Corso, S. de Gironcoli, S. Fabris, G. Fratesi, R. Gebauer, U. Gerstmann, C. Gougoussis, A. Kokalj, M. Lazzeri, L. Martin-Samos, N. Marzari, F. Mauri, R. Mazzarello, S. Paolini, A. Pasquarello, L. Paulatto, C. Sbraccia, S. Scandolo, G. Sclauzero, A. P. Seitsonen, A. Smogunov, P. Umari and R. M. Wentzcovitch, *J. Phys.: Condens. Matter*, 2009, **21**, 395502.
- 31 P. Giannozzi, O. Andreussi, T. Brumme, O. Bunau, M. B. Nardelli, M. Calandra, R. Car, C. Cavazzoni, D. Ceresoli, M. Cococcioni, N. Colonna, I. Carnimeo, A. D. Corso, S. de Gironcoli, P. Delugas, R. A. DiStasio, A. Ferretti, A. Floris, G. Fratesi, G. Fugallo, R. Gebauer, U. Gerstmann, F. Giustino, T. Gorni, J. Jia, M. Kawamura, H.-Y. Ko, A. Kokalj, E. Küçükbenli, M. Lazzeri, M. Marsili, N. Marzari, F. Mauri, N. L. Nguyen, H.-V. Nguyen, A. O. de-la Roza, L. Paulatto, S. Poncé, D. Rocca, R. Sabatini, B. Santra, M. Schlipf, A. P. Seitsonen, A. Smogunov, I. Timrov, T. Thonhauser, P. Umari, N. Vast, X. Wu and S. Baroni, *J. Phys.: Condens. Matter*, 2017, **29**, 465901.
- 32 P. Giannozzi, O. Baseggio, P. Bonfà, D. Brunato, R. Car, I. Carnimeo, C. Cavazzoni, S. de Gironcoli, P. Delugas, F. Ferrari Ruffino, A. Ferretti, N. Marzari, I. Timrov, A. Urru and S. Baroni, *J. Chem. Phys.*, 2020, **152**, 154105.
- 33 D. R. Hamann, *Phys. Rev. B*, 2013, **88**, 085117.
- 34 M. Schlipf and F. Gygi, *Comp. Phys. Commun.*, 2015, **196**, 36–44.
- 35 J. P. Perdew, K. Burke and M. Ernzerhof, *Phys. Rev. Lett.*, 1996, **77**, 3865.
- 36 R. G. Dickinson and L. Pauling, *J. Am. Chem. Soc.*, 1923, **45**, 1466–1471.
- 37 P. B. James and M. Lavik, *Acta Crystallogr.*, 1963, **16**, 1183–1183.
- 38 N. Artrith and A. Urban, *Comp. Mater. Sci.*, 2016, **114**, 135–150.
- 39 A. M. Cooper, J. Kästner, A. Urban and N. Artrith, *npj Comput. Mater.*, 2020, **6**, 54.
- 40 N. Artrith, A. Urban and G. Ceder, *Phys. Rev. B*, 2017, **96**, 014112.
- 41 C. G. Broyden, *J. Inst. Maths. Applics.*, 1970, **6**, 76–90.
- 42 C. Zhu, R. H. Byrd, P. Lu and J. Nocedal, *ACM Trans. Math. Softw.*, 1997, **23**, 550–560.
- 43 A. P. Thompson, H. M. Aktulga, R. Berger, D. S. Bolintineanu, W. M. Brown, P. S. Crozier, P. J. in't Veld, A. Kohlmeyer, S. G. Moore, T. D. Nguyen, R. Shan, M. J. Stevens, J. Tranchida, C. Trott and S. J. Plimpton, *Comp. Phys. Comm.*, 2022, **271**, 108171.
- 44 M. S. Chen, T. Morawietz, H. Mori, T. E. Markland and N. Artrith, *J. Chem. Phys.*, 2021, **155**, 074801.
- 45 J. M. Caillol, D. Levesque and J. J. Weis, *J. Chem. Phys.*, 1986, **85**, 6645–6657.
- 46 S. Nosé, *Molecular Physics*, 1984, **52**, 255–268.
- 47 I. Ponomareva, L. Bellaiche, T. Ostapchuk, J. Hlinka and J. Petzelt, *Phys. Rev. B*, 2008, **77**, 012102.
- 48 H. Tornatzky, R. Gillen, H. Uchiyama and J. Maultzsch, *Phys. Rev. B*, 2019, **99**, 144309.
- 49 T. Tadano, Y. Gohda and S. Tsuneyuki, *J. Phys.: Condens. Matter*, 2014, **26**, 225402.
- 50 C. Lee, H. Yan, L. E. Brus, T. F. Heinz, J. Hone and S. Ryu, *ACS Nano*, 2010, **4**, 2695–2700.
- 51 T. J. Wieting and J. L. Verble, *Phys. Rev. B*, 1971, **3**, 4286–4292.
- 52 A. Garg, H. Sehgal and O. Agnihotri, *Sol. State Commun.*, 1973, **12**, 1261–1263.
- 53 Q.-C. Sun, X. S. Xu, L. I. Vergara, R. Rosentsveig and J. L. Musfeldt, *Phys. Rev. B*, 2009, **79**, 205405.
- 54 T. J. Wieting and J. L. Verble, *Phys. Rev. B*, 1971, **3**, 4286–4292.
- 55 S. Sahoo, A. P. S. Gaur, M. Ahmadi, M. J.-F. Guinel and R. S. Katiyar, *The Journal of Physical Chemistry C*, 2013, **117**, 9042–9047.
- 56 Q. Wang, L. Han, L. Wu, T. Zhang, S. Li and P. Lu, *Nanoscale Research Lett.*, 2019, **14**, 1–9.
- 57 J. Wilson and A. Yoffe, *Adv. Phys.*, 1969, **18**, 193–335.
- 58 S. V. Bhatt, M. P. Deshpande, V. Sathe, R. Rao and S. H. Chaki, *J. Raman Spectrosc.*, 2014, **45**, 971–979.
- 59 S. Najmaei, P. M. Ajayan and J. Lou, *Nanoscale*, 2013, **5**, 9758–9763.
- 60 S. Paul, S. Karak, A. Mathew, A. Ram and S. Saha, *Phys. Rev. B*, 2021, **104**, 075418.
- 61 A. S. Pawbake, M. S. Pawar, S. R. Jadkar and D. J. Late, *Nanoscale*, 2016, **8**, 3008–3018.
- 62 M. Yang, X. Cheng, Y. Li, Y. Ren, M. Liu and Z. Qi, *Appl. Phys. Lett.*, 2017, **110**, 093108.
- 63 N. A. Lanzillo, A. Glen Birdwell, M. Amani, F. J. Crowne, P. B. Shah, S. Najmaei, Z. Liu, P. M. Ajayan, J. Lou, M. Dubey, S. K. Nayak and T. P. O'Regan, *Appl. Phys. Lett.*, 2013, **103**, 093102.
- 64 Z. Li, Y. Lv, L. Ren, J. Li, L. Kong, Y. Zeng, Q. Tao, R. Wu, H. Ma, B. Zhao *et al.*, *Nat. Commun.*, 2020, **11**, 1151.
- 65 H. J. Conley, B. Wang, J. I. Ziegler, R. F. J. Haglund, S. T. Pantelides and K. I. Bolotin, *Nano Lett.*, 2013, **13**, 3626–3630.
- 66 C. Rice, R. J. Young, R. Zan, U. Bangert, D. Wolverson, T. Georgiou, R. Jalil and K. S. Novoselov, *Phys. Rev. B*, 2013, **87**, 081307.
- 67 N. Basu, R. Kumar, D. Manikandan, M. Ghosh Dastidar, P. Hedge, P. K. Nayak and V. P. Bhallamudi, *RSC Adv.*, 2023, **13**, 16241–16247.
- 68 Y. Cai, J. Lan, G. Zhang and Y.-W. Zhang, *Phys. Rev. B*, 2014, **89**, 035438.
- 69 A. Kandemir, H. Yapicioglu, A. Kinaci, T. Çağın and C. Sevik,

- Nanotechnology*, 2016, **27**, 055703.
- 70 T. Sekine, M. Izumi, T. Nakashizu, K. Uchinokura and E. Matsuura, *J. Phys. Soc. Jpn.*, 1980, **49**, 1069–1077.
- 71 M. Jin, W. Zheng, Y. Ding, Y. Zhu, W. Wang and F. Huang, *J. Phys. Chem. Lett.*, 2020, **11**, 4311–4316.
- 72 S. Tongay, J. Zhou, C. Ataca, K. Lo, T. S. Matthews, J. Li, J. C. Grossman and J. Wu, *Nano Lett.*, 2012, **12**, 5576–5580.
- 73 S.-i. Uchida and S. Tanaka, *J. Phys. Soc. Jpn.*, 1978, **45**, 153–161.
- 74 G. Lucovsky, R. M. White, J. A. Benda and J. F. Revelli, *Phys. Rev. B*, 1973, **7**, 3859–3870.
- 75 T. J. Wieting and J. L. Verble, in *Infrared and Raman Investigations of Long-Wavelength Phonons in Layered Materials*, ed. T. J. Wieting and M. Schlüter, Springer Netherlands, Dordrecht, 1979, p. 385.
- 76 A. Garg, H. Sehgal and O. Agnihotri, *Sol. State Commun.*, 1973, **12**, 1261–1263.
- 77 M. Öper, Y. Shehu and N. K. Perkgöz, *Semiconductor Science and Technology*, 2020, **35**, 115020.
- 78 D. Kumar, V. Kumar, R. Kumar, M. Kumar and P. Kumar, *Phys. Rev. B*, 2022, **105**, 085419.
- 79 D. J. Late, S. N. Shirodkar, U. V. Waghmare, V. P. Dravid and C. N. R. Rao, *ChemPhysChem*, 2014, **15**, 1592–1598.
- 80 S. Horzum, H. Sahin, S. Cahangirov, P. Cudazzo, A. Rubio, T. Serin and F. M. Peeters, *Phys. Rev. B*, 2013, **87**, 125415.
- 81 X. Cheng, L. Jiang, Y. Li, H. Zhang, C. Hu, S. Xie, M. Liu and Z. Qi, *Appl. Surf. Sci.*, 2020, **521**, 146398.
- 82 W. Bührer and P. Brüesch, *Phonons: Theory and Experiments II: Experiments and Interpretation of Experimental Results*, Springer Berlin Heidelberg, 2012.
- 83 P. Giannozzi and S. Baroni, *The Journal of chemical physics*, 1994, **100**, 8537–8539.
- 84 X. Gonze and C. Lee, *Phys. Rev. B*, 1997, **55**, 10355.
- 85 H.-P. Komsa, S. Kurasch, O. Lehtinen, U. Kaiser and A. V. Krashennnikov, *Phys. Rev. B*, 2013, **88**, 035301.

Data Availability Statement

All the data that support the conclusions of this study, including the MLFFs presented in this work, the database used for its development and animations for the discussed modes, are available on the following Github Repository:

<https://github.com/gbsouza1997/TMD-MLFF-repo.git>.